
Article:
Forrester, J. orcid.org/0000-0002-8102-7576, Davidson, J.N. and Foster, M.P. (2025) Inductorless step-up piezoelectric resonator (SUPR) converter: a cyclic-mode analysis. IEEE Open Journal of Power Electronics. ISSN: 2644-1314

https://doi.org/10.1109/OJPEL.2025.3646456

This article has been accepted for publication in IEEE Open Journal of Power Electronics. This is the author's version which has not been fully edited and content may change prior to final publication. Citation information: DOI 10.1109/OJPEL.2025.3646456

Inductorless Step-up Piezoelectric Resonator (SUPR) Converter: a Cyclic-Mode Analysis

Jack Forrester, Jonathan N. Davidson, Martin P. Foster

***Abstract*—Cyclic-mode analysis is used to analyse the inductorless step-up piezoelectric-resonator (SUPR) converter. The operation of the converter is decomposed into six operating modes and a non-linear state-variable model is derived. The state-variable model is then transformed into a piecewise linear model based on the operating modes, which can then be subsequently solved in parallel with the optimum operating mode durations using Newton's method. For a set of circuit and piezoelectric resonator (PR) parameters, the proposed model allows various voltages and currents to be estimated. The accuracy of this model is verified against experimental and Simulink results, as well as being compared to state-of-the-art models. The proposed model shows improved accuracy compared to previous models, particularly for low-Q PRs.**

***Index Terms*—DC-DC converters, Design Optimization, Piezoelectric Devices, Resonant Converters, Zero Voltage Switching (ZVS)**

I. INTRODUCTION

PIEZOELECTRIC-BASED power supplies are gaining interest owing to their high efficiency and small volume compared to traditional resonant power supplies. Piezoelectric devices replace most (and, in some cases, all) passive power-stage components from traditional resonant power supplies. This is possible as piezoelectric devices are electrically equivalent to a high-quality-factor and low-loss resonant circuit when driven into vibration near one of their resonant frequencies. Piezoelectric based resonant converters have high power density, have output powers of up to 3.2kW [1], are highly efficient, produce minimal EMI and may be used in harsh environments including high temperature and high magnetic fields [2], [3], [4].

Designing piezoelectric based power supplies is different to traditional magnetic power supplies, as piezoelectric based power supplies rely on mechanical vibration to transform electrical energy. The mechanical properties of piezoelectric devices can be modelled in many ways, including using van Dyke's model of a crystal oscillator, as shown in Fig. 1a.

Modelling, design and control of converters which include a piezoelectric element are therefore different from traditional magnetic converters. Since the behaviour of piezoelectric converter topologies can be significantly different, specific models are required. There is therefore a need to develop specific models to assist with the design of each converter topology taking account of the interaction of electrical and mechanical properties, model fidelity and model simplicity. Owing to the complexity of piezoelectric circuits, there is a need for topology-specific models.

Piezoelectric converters are commonly constructed using piezoelectric transformers (PTs), which are typically two-port devices modelled as a resonant tank connected to an ideal transformer. However, piezoelectric resonator (PR)-based converters are growing in interest due to their increased versatility compared to PT-based converters [5].

PRs are simple in construction, typically formed using only a single layer of piezoelectric ceramic with electrodes on the two main faces, creating a one-port device. When PRs are used in a resonant converter, they act as a resonating energy store, much like the inductor in a boost converter: the PR accumulates and releases energy according to the instantaneous circuit conditions [6]. PRs' resonant properties also allow zero voltage switching (ZVS) to be achieved.

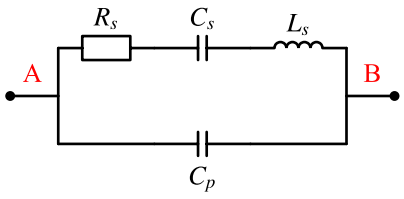

(a)

(b)

Fig. 1 – (a) Piezoelectric resonator equivalent circuit and (b) piezoelectric resonator

The equivalent circuit model of a PR is shown in Fig. 1a, where C_p is the electrode capacitance, C_s and L_s represent the

This work was supported by the Engineering and Physical Sciences Research Council under grant EP/S031421/1. The authors are with the Department of Electronic and Electrical Engineering, University of Sheffield, Sheffield, UK (e-mail:Jack.Forrester@sheffield.ac.uk, Jonathan.Davidson@sheffield.ac.uk, M.P.Foster@sheffield.ac.uk).

This article has been accepted for publication in IEEE Open Journal of Power Electronics. This is the author's version which has not been fully edited and content may change prior to final publication. Citation information: DOI 10.1109/OJPEL.2025.3646456

mechanical resonance and R_s models the damping (loss). Fig. 1b shows an example radial mode PR.

Several authors have developed various PR-based resonant converter topologies for a variety of applications and operating conditions [6], [7], [8], [9], [10], [11], [12], [13]. Boles et al. [5] undertook a substantive analysis of PR converter topologies and switching sequencies, ranking them in terms of PR utilisation and efficiency. A high power PR converter, described in [1], achieved 3.2kW output from parallel connected PR converters.

The SUPR converter introduced in [6] and [14] (shown in Fig. 2) is of particular interest owing to its versatility as it provides both step up and step down power processing capability using only a two-electrode piezoelectric resonator. It is named here as the inductorless step-up piezoelectric resonator (SUPR) converter for convenience. This circuit topology is equivalent to (i) in [5] (operating in synchronous rectification mode), where a comparison of its performance, relative to other PR converters, is found.

In this paper we present a new approach to modelling the SUPR converter using cyclic-mode analysis. Our model provides greater accuracy for low Q factor resonators and provides a 30% improvement over the describing function-based model in [15], which is limited to sinusoidal resonant currents, an assumption which is not valid for low Q factor PRs.

Section II discusses the operation of the SUPR converter. The cyclic-mode analysis method described in [16], [17] is adapted by augmenting the state vector with additional expressions that describe the commutation events that represent the mode transitions. This augmented cyclic model is described in sections III and IV. Results from the proposed model are compared to the models in [6] and [15], as well as experimental and Simulink results for a prototype converter design in section V.

II. SUPR CONVERTER AND ITS OPERATION

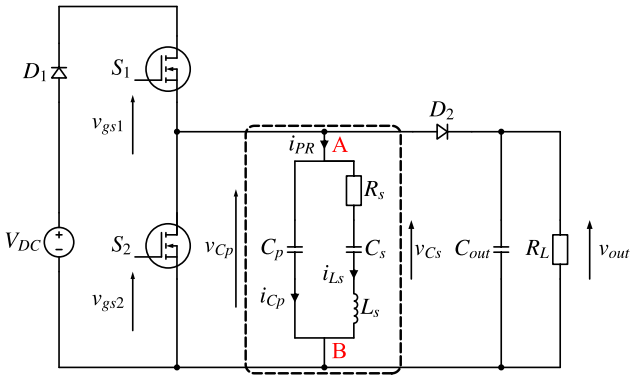

Fig. 2 – Piezoelectric-resonator-based boost converter

Fig. 2 shows the circuit diagram for the step-up piezoelectric-resonator (SUPR) converter. The operating waveforms for the converter are shown in Fig. 3 where the voltages v_{C_p} and v_{out} are shown normalised to the input voltage V_{DC}. The start of a cycle ($t = t_0$) is defined as the positive zero crossing of current (i_{L_s}). A cycle is divided into six modes of operation (circuit configurations) depending on the conduction states of the diodes and the control of the MOSFET switches. The circuit is driven at an operating frequency f such with a period $T = 1/f = 2\pi/\omega$.

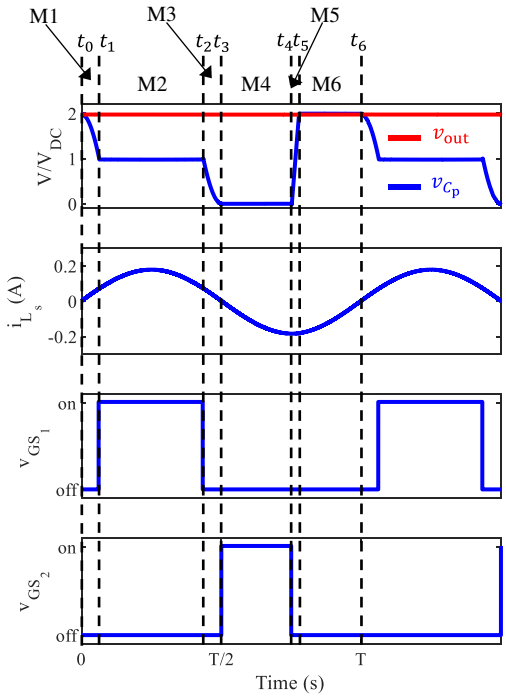

Fig. 3 – Typical operating waveforms for the SUPR converter

The six modes of operation M1→M6 for this converter during typical operation are: —

M1 ($t_0 \rightarrow t_1$): Prior to start of a cycle, $v_{C_p}(t_0) = v_{out} + V_{df}$, where v_{out} is the output voltage (and is greater than the input voltage V_{DC}) and V_{df} is the forward voltage drop of D_1 and D_2. Both MOSFETs S_1 and S_2 are turned off at $t = t_0$, as the current i_{L_s} undergoes a positive zero crossing. During M1, $i_{L_s} = -i_{C_p}$ circulates within the PR, discharging C_p and causing v_{C_p} to decrease until it reaches $V_{DC} - V_{df}$. Since $v_{C_p} < v_{out}$, D_2 is reverse-biased and so C_{out} provides the energy to the load.

M2 ($t_1 \rightarrow t_2$): At t_1, S_1 is turned on with zero voltage across it (ZVS), clamping $v_{C_p} = V_{DC} - V_{df}$. Energy is supplied to the resonator through S_1 during M2.

M3 ($t_2 \rightarrow t_3$): Both S_1 and S_2 are turned off, $i_{L_s} = -i_{C_p}$ circulates within the PR discharging C_p.

M4 ($t_3 \rightarrow t_4$): At t_3, i_{L_s} undergoes a negative zero crossing and switch S_2 is turned on (ZVS). During M4, $v_{C_p} = -i_{L_s} R_{DS_{on}}$ as i_{L_s} flows through S_2.

M5 ($t_4 \rightarrow t_5$): At t_4, S_2 is turned off, the negative i_{L_s} charges C_p thereby increasing v_{C_p}.

M6 ($t_5 \rightarrow t_6$): At t_5, D_2 becomes forward-biased, thus energy is provided from the resonator to R_L and C_{out}. During M6, $v_{C_p} = v_{out} + V_{df}$.

The duration of M4 is used to control the voltage gain of the converter. For this analysis, we will assume $(t_4 - t_3)/T = \delta_4$ is fixed. Subsequently, the unknown mode transition times (t_1,

t_2, t_3 and t_5) and switching period T are dependent on the PR parameters and circuit operation, and so are to be found.

In [15] we showed that the SUPR converter can achieve ZVS over a wide variety of operating conditions if a suitable controller is used. A model for the SUPR converter when used in a step-up configuration was developed using a describing function approach. This model allows the optimum switch duty cycles to be determined and various voltages and currents of interest to be estimated for a given PR and converter specification. The describing function-based model showed good accuracy when evaluated against experimental and simulation results, improving on the state of the art. However, the model is complex to solve, requiring the use of non-linear solving algorithms. For low Q factor PRs the current is distorted (non-sinusoidal), thereby reducing the validity of the assumptions made in the describing function. This is shown in Fig. 9.

III. Derivation of Cyclic-mode model

A common technique for analysing resonant circuits is cyclic modelling [16], [17], [18], [19]. This technique decomposes the operation of the circuit into a series of operating modes. It is assumed that the converter operates cyclically such that state vector $x(t)$ (comprising of relevant voltages and currents) is periodic in T such that

$$\boldsymbol{x}(t) = \boldsymbol{x}(t+T) \tag{1}$$

By utilising the cyclic-mode behaviour, authors show that the value of the state vector can be estimated from equations without integration. As a result, it is comparatively rapid to compute whilst showing excellent accuracy.

For the SUPR converter defining the state vector as $\boldsymbol{x} = [v_{C_\mathrm{s}} \quad v_{C_\mathrm{p}} \quad i_{L_\mathrm{s}} \quad v_{\mathrm{out}}]^T$, then the cyclic-mode steady state for the SUPR converter occurs if $\boldsymbol{x}(t_6) = \boldsymbol{x}(t_0)$. For a DC-DC converter, where the input voltage is assumed constant, this condition can be modelled using the cyclic-mode analysis technique described in [17] where the behaviour of the converter is described by a piecewise-linear state-variable model of the form

$$\dot{\boldsymbol{x}} = \boldsymbol{A}_i\boldsymbol{x} + \boldsymbol{B}_i \tag{2}$$

where $\boldsymbol{A}_i$ is the dynamic matrix and $\boldsymbol{B}_i$ is the corresponding input matrix for mode Mi. For a given mode, Mi, the state vector $\boldsymbol{x}(t)$ (where $t_{i-1} \le t < t_i$) can be found by solving (2) giving,

$$\boldsymbol{x}(t) = \exp\big(\boldsymbol{A}_\mathrm{i}(t-t_{i-1})\big)\boldsymbol{x}(t_{i-1}^+) + \int_{t_{i-1}}^{t_i} \exp\big(\boldsymbol{A_i}(t-\tau)\big)\,\boldsymbol{B}_i\,d\tau \tag{3}$$

$\boldsymbol{x}(t_{i-1}^+)$ represents the initial value of the state vector during mode i and $\boldsymbol{x}(t_{i-1}^-)$ represents the value of the state vector at the end of mode $i-1$. t_{i-1}^+ represents the instant after t_{i-1}^-, this distinction allows the modelling of discontinuity between the boundaries of modes.

A constant input matrix $\boldsymbol{B}$ simplifies the integration necessary to evaluate (1). The solution for $\boldsymbol{x}$ at time t_i with this assumption is given by

$$\boldsymbol{x}(t_i) = \boldsymbol{\Phi_i}\boldsymbol{x}(t_{i-1}) + \boldsymbol{\Gamma}_i \tag{4}$$

where $\boldsymbol{\Phi}_i = \exp\,[\boldsymbol{A}_i(t_i - t_{i-1})]$ is the state-transition matrix, $\boldsymbol{\Gamma}_i = \boldsymbol{A}_i{}^{-1}[\boldsymbol{\Phi}_i - \boldsymbol{I}]\mathbf{B}_i$, $\boldsymbol{I}$ is the identity matrix and $\boldsymbol{x}(t_{i-1})$ is the initial condition for the i^{th} mode.

A more convenient form for (4) can be obtained by introducing a dynamic matrix $\widetilde{\boldsymbol{A}}_\boldsymbol{i}$ which augments $\boldsymbol{A_i}$ and $\boldsymbol{B_i}$ to provide a new system representation

$$\widetilde{\boldsymbol{x}}(t_i) = \widetilde{\boldsymbol{\Phi}}_\boldsymbol{i}\widetilde{\boldsymbol{x}}(t_{i-1}) \tag{5}$$

where

$$\widetilde{\boldsymbol{\Phi}}_\boldsymbol{i} = \exp\,[\widetilde{\boldsymbol{A}}_\boldsymbol{i}(t_i - t_{i-1})] \tag{6}$$

$$\widetilde{\boldsymbol{A}}_i = \begin{bmatrix} \boldsymbol{A_i} & \boldsymbol{B_i} \\ 0 & 0 \end{bmatrix} \tag{7}$$

$$\widetilde{\boldsymbol{x}} = \begin{bmatrix} \boldsymbol{x} \\ 1 \end{bmatrix} \tag{8}$$

Using (5), the value of the state vector at the end of the cycle can be found by cascading the solutions for each mode. Since the SUPR converter operates with six modes per cycle,

$$\begin{aligned} \widetilde{\boldsymbol{x}}(t_6) &= \widetilde{\boldsymbol{\Phi}}_\boldsymbol{6}\widetilde{\boldsymbol{\Phi}}_\boldsymbol{5}\widetilde{\boldsymbol{\Phi}}_\boldsymbol{4}\widetilde{\boldsymbol{\Phi}}_\boldsymbol{3}\widetilde{\boldsymbol{\Phi}}_\boldsymbol{2}\widetilde{\boldsymbol{\Phi}}_\boldsymbol{1}\widetilde{\boldsymbol{x}}(t_0) \\ &= \widetilde{\boldsymbol{\Phi}}_{\boldsymbol{tot}}\widetilde{\boldsymbol{x}}(t_0) \\ &= \begin{bmatrix} \boldsymbol{\Phi_{tot}} & \boldsymbol{\Gamma_{tot}} \\ 0 & 1 \end{bmatrix}\begin{bmatrix} \boldsymbol{x}(t_0) \\ 1 \end{bmatrix} \end{aligned} \tag{9}$$

The cyclic-mode initial state is related to the final state by

$$\widetilde{\boldsymbol{x}}(t_6) \equiv \widetilde{\boldsymbol{x}}(t_0 + T) = \widetilde{\boldsymbol{x}}(t_0) \tag{10}$$

Applying (8) and (10) to (9) and solving for the state vector provides the cyclic-mode initial condition,

$$\boldsymbol{x}(t_0) = [\boldsymbol{I} - \boldsymbol{\Phi_{tot}}]^{-1}\boldsymbol{\Gamma_{tot}} \tag{11}$$

The value of the state vector at time t where $t_{i-1} \le t < t_i$ can then be calculated using (5), (11) and

$$\widetilde{\boldsymbol{x}}(t) = \exp\left(\widetilde{\boldsymbol{A}}_\boldsymbol{i}(t - t_{i-1})\right)\widetilde{\boldsymbol{x}}(t_{i-1}^+) \tag{12}$$

where $\widetilde{\boldsymbol{x}}(t_{i-1}^+)$ is the value of the augmented state vector at the start of mode i. If ZVS is not achieved, then discontinuities in v_{C_p} occur at the beginning of M2 and M4 due to MOSFET switching. To account for this, $\widetilde{\boldsymbol{x}}(t_1^+)$ and $\widetilde{\boldsymbol{x}}(t_3^+)$ can be defined as

$$\widetilde{\boldsymbol{x}}(t_1^+) = \boldsymbol{K}\widetilde{\boldsymbol{x}}(t_1^-) + [0 \quad (V_{\mathrm{DC}} + V_{\mathrm{df}}) \quad 0 \quad 0 \quad 0] \tag{13}$$

$$\widetilde{\boldsymbol{x}}(t_3^+) = \boldsymbol{K}\widetilde{\boldsymbol{x}}(t_3^-) \tag{14}$$

where $\boldsymbol{K}$ is given by,

This article has been accepted for publication in IEEE Open Journal of Power Electronics. This is the author's version which has not been fully edited and content may change prior to final publication. Citation information: DOI 10.1109/OJPEL.2025.3646456

$$\boldsymbol{K}=\begin{bmatrix}1&0&0&0&0\\0&0&0&0&0\\0&0&1&0&0\\0&0&0&1&0\\0&0&0&0&1\end{bmatrix} \tag{15}$$

IV. Piecewise Linear Model

A state-variable model for the SUPR converter is now derived from the differential equations for the inductor current (i_{L_s}) and the three capacitor voltages ($v_{C_s}, v_{C_p}, v_{out}$). From these differential equations, a piecewise linear model is presented based on operating characteristics discussed in section II.

A. State-variable model derivation

The first derivative of the inductor current $\dot{i_{L_s}}$ is given by,

$$\frac{d}{dt}i_{L_s}=\dot{i_{L_s}}=\frac{v_{C_p}-v_{C_s}-i_{L_s}R_s}{L_s} \tag{16}$$

For the resonant capacitor voltage,

$$\dot{v_{C_s}}=\frac{i_{L_s}}{C_s} \tag{17}$$

For the parallel capacitor voltage,

$$\dot{v_{Cp}}=\begin{cases}-\dfrac{i_{L_s}}{C_p} & \text{M1, M3, M5}\\ \dot{v_{out}} & \text{M6}\\ \dfrac{h(V_{DC}-V_{df})-v_{C_p}-R_{DS}i_{L_s}}{R_{DS}C_P} & \text{M2, M4}\end{cases} \tag{18}$$

where h describes the on state of S_1,

$$h=\begin{cases}1, & \text{M2}\\ 0, & \text{otherwise}\end{cases} \tag{19}$$

It should be noted that the expression for $\dot{v}_{C_p}$ during M6 does not depend on the diode voltage drop, a full derivation is detailed in the appendix.

Finally,

$$\dot{v_{out}}=\begin{cases}-\dfrac{i_{L_S}}{C_{out}+C_p}-\dfrac{v_{out}}{(C_{out}+C_p)R_L} & \text{M6}\\ -\dfrac{v_{out}}{C_{out}R_L} & \text{Otherwise}\end{cases} \tag{20}$$

A full derivation of (20) is shown in the appendix.

B. Decomposition into piecewise linear models

A piecewise linear model is now derived from the non-linear dynamic model described in previous section and is of the form,

$$\dot{x}=\begin{cases}\boldsymbol{A_1x}+\boldsymbol{B}_1, & t_0\le t<t_1\\ \vdots & \vdots\\ \boldsymbol{A}_6\boldsymbol{x}+\boldsymbol{B}_6 & t_5\le t<t_6\end{cases} \tag{21}$$

Based on equations (16)-(20), dynamic $\boldsymbol{A}_i$ and input $\boldsymbol{B}_i$ matrices for each mode are defined as

$$\boldsymbol{A}_1=\boldsymbol{A}_3=\boldsymbol{A}_5=\begin{bmatrix}0&0&\frac{1}{C_s}&0\\0&0&-\frac{1}{C_p}&0\\-\frac{1}{L_s}&\frac{1}{L_s}&-\frac{R_s}{L_s}&0\\0&0&0&-\frac{1}{C_{out}R_L}\end{bmatrix} \tag{22}$$

$$\boldsymbol{A}_2=\boldsymbol{A}_4=\begin{bmatrix}0&0&\frac{1}{C_s}&0\\0&-\frac{1}{R_{DS}C_P}&-\frac{1}{C_p}&0\\-\frac{1}{L_s}&\frac{1}{L_s}&-\frac{R_s}{L_s}&0\\0&0&0&-\frac{1}{C_{out}R_L}\end{bmatrix} \tag{23}$$

$$\boldsymbol{A}_6=\begin{bmatrix}0&0&\frac{1}{C_s}&0\\0&0&-\frac{1}{C_{out}+C_p}&-\frac{1}{(C_{out}+C_p)R_L}\\-\frac{1}{L_s}&\frac{1}{L_s}&-\frac{R_s}{L_s}&0\\0&0&-\frac{1}{C_{out}+C_p}&-\frac{1}{(C_{out}+C_p)R_L}\end{bmatrix} \tag{24}$$

$$\boldsymbol{B}_1=\boldsymbol{B}_3=\boldsymbol{B}_4=\boldsymbol{B}_5=\boldsymbol{B}_6=[0\quad 0\quad 0\quad 0]^T \tag{25}$$

$$\boldsymbol{B}_2=\begin{bmatrix}0&\frac{V_{DC}-V_{df}}{R_{DS}C_P}&0&0\end{bmatrix}^T \tag{26}$$

Note here that we have assumed that the two MOSFETs are identical. Using (12) with (21)-(26) and the initial conditions calculated using (9) and (11), and knowledge of the durations of each of the modes, the value of the state vector can be calculated at any time. Thus, this allows the full waveform for each of the state variables to be calculated.

However, the mode durations (i.e. for mode i, the duration is given by t_i-t_{i-1}) and the operating frequency are unknown and need to be determined.

C. Determining the mode durations

The method in [15] is used to make an initial estimate of the mode durations and subsequently $\boldsymbol{x}(t_0)$. Then the shooting method presented in [20] is used to refine the estimate of both the mode durations and $\boldsymbol{x}(t_0)$ simultaneously.

For the SUPR converter, the operation of the converter across the whole cycle is dependent on the cyclic mode initial conditions, the mode durations, and the switching period.

Therefore, we define an augmented vector $\boldsymbol{X}$ containing the state-variables and the unknown mode duties,

$$\boldsymbol{X} = [\boldsymbol{x}(t_0)^{\mathrm{T}} \quad | \quad \delta_1 \quad \delta_2 \quad \delta_3 \quad \delta_5 \quad T]^{\mathrm{T}} \tag{27}$$

where $\delta_i = (t_i - t_{i-1})/T$ is the duty cycle of mode i, it should be noted that δ_4 is a control input.

When the SUPR converter is operating in steady state, there are several conditions that define the end of each mode. At the end of M1,

$$v_{C_\mathrm{p}}(t_1^- = \delta_1 T) = V_{\mathrm{DC}} - V_{\mathrm{df}} \tag{28}$$

The duration of M2 is set, such that at the end of M3,

$$v_{C_\mathrm{p}}\left(t_3^- = \sum_{i=1}^{3} \delta_i\, T\right) = 0 \tag{29}$$

Where $\sum_{i=1}^{n} \delta_i$is the sum of duty ratios from 1 to mode n. The inductor current should be zero at the end of M3,

$$i_{L_\mathrm{s}}\left(t_3^- = \sum_{i=1}^{3} \delta_i\, T\right) = 0 \tag{30}$$

At the end of M5,

$$v_{C_\mathrm{p}}\left(t_5^- = \sum_{i=1}^{5} \delta_i\, T\right) = V_{\mathrm{out}} - V_{\mathrm{df}} \tag{31}$$

Finally, with the correct switching period T,

$$i_{L_\mathrm{s}}(t_6^- = T) = 0 \tag{32}$$

Based on these conditions, we define a cost vector $\boldsymbol{G}$ which is a function of $\boldsymbol{X}$ such that, when each of the aforementioned conditions is fulfilled, $\boldsymbol{G}(\boldsymbol{X}) = \boldsymbol{0}$,

$$\boldsymbol{G}(\boldsymbol{X}) = \begin{bmatrix} \boldsymbol{x}(t_0 + \mathrm{T}) - \boldsymbol{x}(t_0) \\ \hline v_{C_\mathrm{p}}(t_1^-) - V_{\mathrm{DC}} + V_{\mathrm{df}} \\ v_{C_\mathrm{p}}(t_3^-) \\ i_{L_\mathrm{s}}(t_3^-) \\ v_{C_\mathrm{p}}(t_5^-) - V_{\mathrm{out}} - V_{\mathrm{df}} \\ i_{L_\mathrm{s}}(t_6^-) \end{bmatrix} = \begin{bmatrix} g_1 \\ g_2 \\ g_3 \\ g_4 \\ \hline g_5 \\ g_6 \\ g_7 \\ g_8 \\ g_9 \end{bmatrix} \tag{33}$$

Newton's method is then used iteratively to estimate the true value of $\boldsymbol{X}$**.** The matrix form of Newton's method used in this work is defined as

$$\boldsymbol{X}^k = \boldsymbol{X}^{k-1} - \alpha\left[\boldsymbol{J}\left(\boldsymbol{G}(\boldsymbol{X}^{k-1})\right)\right]^{-1}\boldsymbol{G}(\boldsymbol{X}^{k-1}) \tag{34}$$

where α is a relaxation factor with a value $0 < \alpha \leq 1$, which improves the convergence, k is the index of the current iterative step and $\boldsymbol{J}\left(\boldsymbol{G}(\boldsymbol{X}^{k-1})\right)$ is the 9 x 9 Jacobian matrix of the function $\boldsymbol{G}(\boldsymbol{X})$. The Jacobian matrix is defined as

$$\boldsymbol{J}\left(\boldsymbol{G}(\boldsymbol{X})\right) = \frac{\partial \boldsymbol{G}}{\partial \boldsymbol{X}} = \begin{bmatrix} \frac{\partial g_1}{\partial X_1} & \cdots & \frac{\partial g_1}{\partial X_9} \\ \vdots & \ddots & \vdots \\ \frac{\partial g_9}{\partial X_1} & \cdots & \frac{\partial g_9}{\partial X_9} \end{bmatrix} \tag{35}$$

Given the complexity of finding the partial derivatives within $\boldsymbol{J}\left(\boldsymbol{G}(\boldsymbol{X})\right)$, it is more convenient to estimate $\boldsymbol{J}\left(\boldsymbol{G}(\boldsymbol{X})\right)$, where partial derivatives are calculated using

$$\frac{\partial g_u(\boldsymbol{X})}{\partial X_v} \approx \frac{g_u(\boldsymbol{X} + \Delta \boldsymbol{X}_v) - g_u(\boldsymbol{X})}{\beta_v} \tag{36}$$

where u and v are the row and column indices respectively of the matrix in (35), $\Delta \boldsymbol{X}_v = [0 \quad \cdots \quad \beta_v \quad \cdots \quad 0]^T$ is a 9 x 1 vector with a small perturbation β_v in the v^{th} position. In this work, we chose $\beta_v = 1 \times 10^{-8}$. After several iterations and with a suitable initial estimate $\boldsymbol{X}^0$, $\boldsymbol{X}$ will converge on the true initial conditions, such that,

$$|\boldsymbol{X}^{k_{\mathrm{final}}} - \boldsymbol{X}^{k_{\mathrm{final}}-1}|_2 < \lambda \tag{37}$$

where $|.|_2$ is the L^2-norm, $X^{k_{final}}$ is the final value of $\boldsymbol{X}$ and λ is an acceptably small value. In this work, we chose $\lambda = 1 \times 10^{-10}$. Therefore, using $\boldsymbol{X}^{k_{final}}$ with (12) and (21)-(26), the value of the state vector $\boldsymbol{x}(t)$ can be calculated at any time within the cycle.

V. Model Verification

The accuracy of the proposed model will be compared against experimentally collected data and Simulink simulations.

A. *Validation methodology*

The model is validated against three parameter variations (δ_4, load and piezo resonator Q factor).

1) *Duty cycle - δ_4*

The proposed model is used to estimate the voltage gain $\left(M_{\mathrm{out}} = (V_{\mathrm{DC}}T)^{-1}\int_0^T v_{\mathrm{out}}\, dt\right)$ of a SUPR converter with PR equivalent circuit properties given in Table 1 and when driven over the range $\delta_4 = [0.15,\ 0.35]$ with a fixed 1kΩ load. Subsequently experimental and Simulink measurements are collected under the same conditions, allowing the accuracy of the voltage gain estimated. A further comparison is made with the describing function model presented in [15] and model developed in [6].

2) *Load - R_L*

The accuracy of the voltage gain as a function of load estimated by the cyclic model will be validated in the range $R_L = [500\Omega,\ 20\mathrm{k}\Omega]$ with a fixed $\delta_4 = 0.26$.

3) *Q factor*

Finally, one of the benefits of the cyclic model compared to describing function modelling, is the removal of the assumption that the first harmonic dominates the resonant current. Some piezoelectric materials exhibit low Q factors (for example, BSPT for use in high temperature [21] applications). The

bandpass filtering properties of low Q materials are inferior to high Q materials (such as PZT) meaning that the resonant current is no longer sinusoidal, and this invalidates a key assumption for the describing function approach. Therefore, the estimated v_{C_p} waveform for both the proposed model and the describing function model [15] are compared against a Simulink simulation of a low Q factor PR based SUPR converter. It should be noted that the model in [6] does not allow estimation of the v_{C_p} waveform and therefore was omitted from this result.

B. Experimental setup

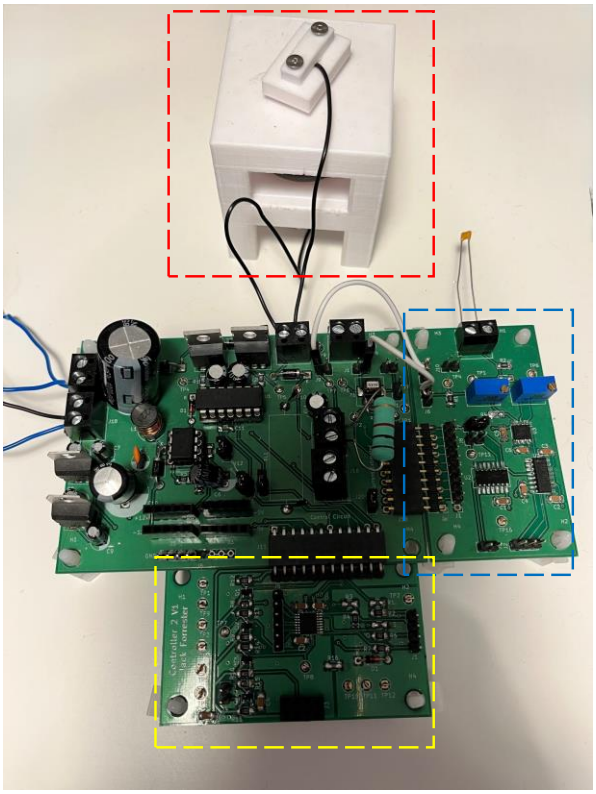

Fig. 4 - SUPR Converter. Radial PR in 3D printed mount (red), current estimator circuitry (blue) and FPGA connections with signal processing (yellow)

Table 1 - SMD30T21F1000S properties

Material	Vibration mode	Diameter (mm)	Thickness (mm)
SM112	Radial	30	2.1
R_s	L_s	C_s	C_p
2.22 Ω	4.47 mH	1.02 nF	2.54 nF

A SUPR converter (shown in Fig. 4) is constructed using a SMD30T21F1000S PR from Steminc as shown in Fig. 1b. The physical properties of the resonator and equivalent circuit component values that were extracted using the characterisation technique described in [22] are given in Table 1.

1) Hardware

A hardware circuit diagram is shown in Fig. 5. The main SUPR converter comprises MOSFETs S1 and S2 (IRF510), which are driven by a half-bridge gate driver IC (IR2110). D_1 and D_2 are low forward voltage Schottky diodes (1N5819). The SUPR converter is completed with an output capacitance $C_{\text{out}} = 10$ µF and a DC input voltage $V_{\text{DC}} = 12$ V.

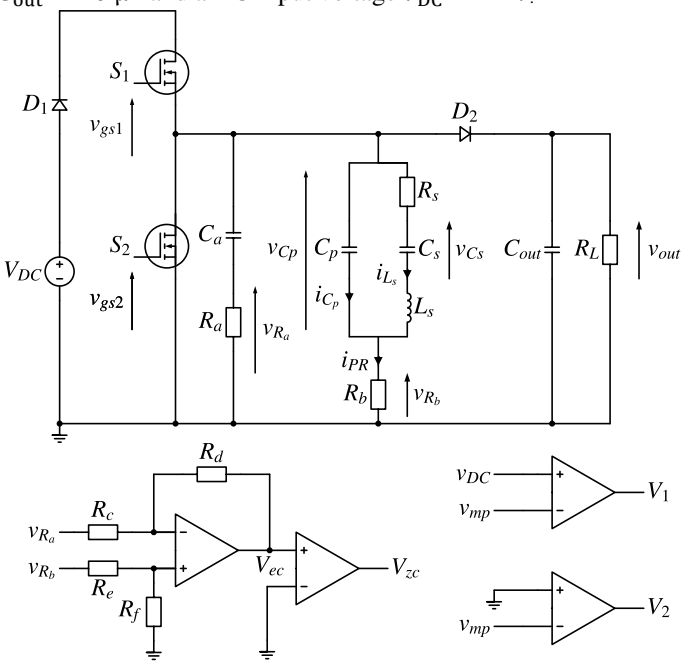

Fig. 5 - SUPR hardware circuit diagram

It is well documented that the resonant current cannot be directly electrically measured in piezoelectric devices, thus the current estimator presented in [23] was used to determine the resonant current. The resonator current is defined as $i_{\text{PR}} = i_{C_{\text{p}}} + i_{L_s}$. Therefore, by connecting an external RC branch (C_a and R_a) in parallel with the resonator, a voltage proportional to $i_{C_{\text{p}}}$ (viz. V_{R_a} in Fig. 5) can be estimated. An instrumentation amplifier U1 then subtracts V_{R_a} from $V_{\text{R}_\text{b}} = i_{\text{PR}} R_b$, creating a voltage V_{ec} which is proportional to resonant current i_{L_s}.

Since only zero crossings of i_{L_s} are required by the controller, comparator U2 detects the zero crossing of V_{ec} producing a square wave output voltage V_{zc}. V_{zc} is the input to the FPGA-based PLL; the PLL output is the square-wave PLL_{out} in Fig. 6. When the PLL has achieved lock, PLL_{out} will be in-phase with V_{zc} and synchronised to the zero crossing of the resonant current of the PR. Two additional comparators are required to sense the end of M1 and M2. This is accomplished using comparators U3 and U4 (MAX9203), which produce $V_1 = \text{sgn}\left(v_{C_{\text{p}}} - V_{\text{DC}}\right)$ and $V_2 = -\text{sgn}\left(v_{C_{\text{p}}}\right)$.

2) Software and programmable logic (FPGA)

Based on the hardware design, an FPGA takes inputs V_{zc}, V_1 and V_2, and produces gate signals G1 and G2 to drive the two MOSFET switches. A Digilent PYNQ FPGA development was used, which features a Xilinx ZYNQ FPGA. ZYNQ FPGAs are made up of 2 parts, programmable logic which is the FPGA component and the processing system which is a processor core running Linux. This development board allows the programmable logic to interface to the processing system using the Python programming language. In this application, the

This article has been accepted for publication in IEEE Open Journal of Power Electronics. This is the author's version which has not been fully edited and content may change prior to final publication. Citation information: DOI 10.1109/OJPEL.2025.3646456

programmable logic performs all the computation required to generate the corresponding output signals to drive the SUPR converter and the processing system is used to provide manual input to the programmable logic to control the δ_4 duty cycle and, thus, the gain of the converter. A full explanation of the hardware and software can be found in [24].

3) *Experimental waveforms*

Experimental waveforms for the prototype converter with a 1 kΩ load, a 12 V DC input voltage and with $\delta_4 = 0.26$ are shown in Fig. 6.

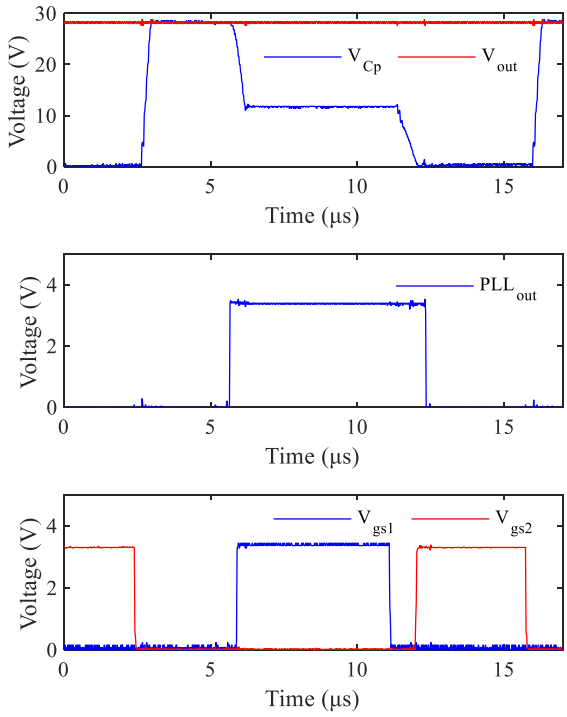

Fig. 6 – Experimental waveforms for the prototype converter when operated with a 1kΩ load and $\delta_4 = 0.26$

C. *Simulink simulation setup*

The SUPR converter was modelled and simulated in Simulink using the Simscape package, with the MOSFETs driven by a state machine controller created using the Stateflow package. The state machine has 5 states which correspond to the 6 different operating modes of the converter (described in Section II), this is detailed in Table 2. M6 differs from M5 only by the conduction state of D_2 therefore both modes correspond to State 5.

Table 2 - State machine states

State	Mode	Switches		Condition for start of state
		S1	S2	
State 1	M1	Off	Off	V_{zc} rising edge
State 2	M2	On	Off	V_1 rising edge
State 3	M3	Off	Off	$\delta_3 T$ after State 2
State 4	M4	Off	On	V_{zc} falling edge
State 5	M5	Off	Off	$\delta_4 T$ after State 4
	M6	Off	Off	

For the first 1µs of operation the states are fixed length in order to establish the resonant behaviour. After 1µs, the controller dynamically controls the mode durations based on the measured v_{C_P} and i_{L_S}.

The state transition conditions are shown in Table 2. There are two defined period states, State 3 and State 5. The duration of State 3, $\delta_3 T$ is adjusted incrementally each cycle to minimise the $v_{C_p}(t_3)$ according to (38).

$$[\delta_3 T]^{k+1} = [\delta_3 T]^k + \begin{cases} \lambda \operatorname{sgn}\left(v_{C_p}(t_3)\right), & \left|v_{C_p}(t_3)\right| > 0.1 \\ 0, & \text{otherwise} \end{cases} \quad (38)$$

where k is index of the present cycle and $\lambda = 1$ ns is a small timestep. In the open loop implementation in this paper, δ_4 is used as the independent variable to produce the results.

The MOSFET on-state resistance ($R_{DS} = 0.54\Omega$) and the diode forward voltage drop ($V_{df} = 0.3$V) was set to match the experimental devices chosen. Simulation ran until the converter reached steady state.

D. *Comparison between simulation results and experiment experiments*

1) *Changes in S_2 duty cycle δ_4*

Fig. 7 shows the voltage gain predicted by the proposed cyclic model, the describing function model from [15], the model described in [6] (using frequencies calculated using the proposed cyclic model), Simulink simulations and experimental measurements as a function of δ_4, when driving a 1kΩ load. Converter efficiency estimated by the model varies between 67-92% (0.2-2W output power), depending on duty, with lower duties giving higher efficiency.

The voltage gain estimated by the cyclic model and other models closely matches the experimental and Simulink measurements at low δ_4. At high δ_4, the cyclic model overestimates the voltage gain of the converter, when compared to Simulink results. Compared to the describing function model previously published [15], a lower average absolute error in gain is achieved by the cyclic mode model (1.07% vs 1.44%) when compared to experimental results. Additionally, the cyclic model is significantly more accurate than the model described in [6], particularly at high δ_4 values.

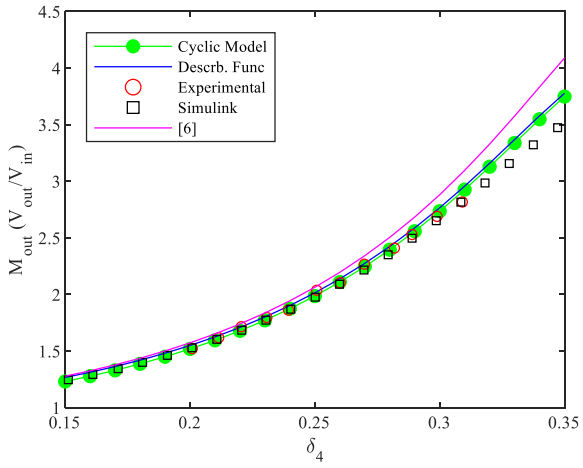

Fig. 7 - Voltage gain against δ_4, with a 1kΩ load

This article has been accepted for publication in IEEE Open Journal of Power Electronics. This is the author's version which has not been fully edited and content may change prior to final publication. Citation information: DOI 10.1109/OJPEL.2025.3646456

2) Changes in load

Fig. 8 shows the voltage gain predicted by the cyclic model, describing function model in [15], the model in [6] (again using frequencies calculated using the proposed model), Simulink simulations and experimental results with changes in load, when driven with $\delta_4 = 0.26$. Converter efficiency estimated by the model varies between 84-93% (0.23-1W output power), depending on load, with maximum efficiency occurring with 5.8kΩ load.

The cyclic model shows good accuracy compared to experimental results, with a lower average absolute error (1.84% vs 2.03%) than the describing function model, when compared to experimental results. At higher load resistances, the cyclic model estimates lower gains than to the describing function model; thus, the cyclic mode shows better agreement with the experimental results.

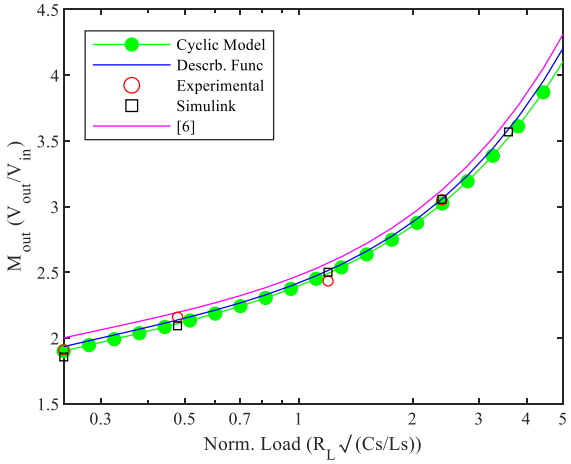

Fig. 8 - Voltage gain against load, with $\delta_4 = 0.26$

3) Changes in Q factor

In our previous work [15], we investigated the accuracy of the describing function model against changes in PR equivalent circuit parameters (R, C_p, F_0 and $Z_0 = \sqrt{L/C}$) compared to LTSpice simulations. In the study it was found that changes in R, C_p and F_0 have minimal effect on the accuracy of the model, however, decreasing Z_0 ($\propto$ Q factor) caused a significant reduction in model accuracy. This is because the accuracy of describing function models diminishes in the presence of harmonics, which occur in lower Q tanks. The proposed cyclic model remains accurate for non-sinusoidal waveforms.

Fig. 9 shows transient waveforms for a circuit with a low-Q PR using the proposed cyclic model, describing function model and Simulink. Table 3 shows the equivalent circuit parameters of the PR, with Z_0 set to 1/10 of the original value (210 Ω vs 2.1 kΩ) of the SMD30T21F1000S PR.

Table 3 – Low Z_0 PR equivalent circuit properties

R_s	L_s	C_s	C_p
2.22 Ω	447 µH	10.2 nF	2.54 nF

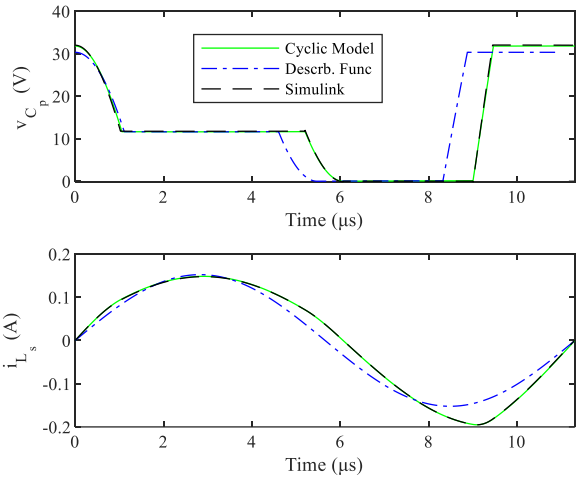

Fig. 9 - v_{C_p} and i_{L_s} from Simulink and predicted by the proposed cyclic mode and describing function model, with $\delta_4 = 0.26$

Fig. 9 shows that, when compared to Simulink, the cyclic model produces a significantly more accurate result than the describing function model. The cyclic model and Simulink produce a non-sinusoidal current, in contrast to the describing function model. As the waveform shape is different, the timings of the state transition conditions are closer to the intended values.

Table 4 shows the percentage error in voltage gain, resonant current amplitude, and duty cycles for each model. The cyclic model shows excellent correspondence, with the highest error for any parameter being 2.37% (in most cases less than <1%). Conversely, the describing function model shows increased error in most parameters compared to the cyclic model, with errors up to 30%. This analysis proves the benefit of the cyclic model, as it is significantly more accurate than the describing function model when applied to lower Z_0 PRs.

Table 4 - Percentage error between Simulink, and cyclic and describing function models

	Simulink	Cyclic Model Error	Describing Function Model Error
M_{out}	2.65	0.91%	5.54%
$i_{L_{s_{max}}}$	0.15	0.46%	3.11%
$i_{L_{s_{min}}}$	-0.20	0.03%	21.95%
$i_{L_{s_{RMS}}}$	0.12	0.27%	9.73%
δ_1	0.091	2.37%	11.33%
δ_2	0.369	0.62%	13.56%
δ_3	0.077	0.17%	0.78%
δ_5	0.040	2.03%	30.27%
T	11.3µs	0.09%	3.22%

VI. Conclusion

A cyclic-mode model of the SUPR converter is presented. The operation of the converter is decomposed into six operating modes and a piecewise linear model is derived. Based on the piecewise linear model, cyclic mode analysis is performed and the application of Newton's method for determining initial conditions and mode durations is presented. The cyclic-mode model is then validated against experimental and Simulink results and compared to previous models presented in [6], [15]. The cyclic-mode model presented here shows excellent accuracy, improving on previous models, especially for low Q factor (low Z_0) PRs.

VII. References

[1] E. Stolt, W. Braun, K. Nguyen, V. Chulukhadze, R. Lu, and J. Rivas-Davila, 'A Spurious-Free Piezoelectric Resonator Based 3.2 kW DC–DC Converter for EV On-Board Chargers', *IEEE Transactions on Power Electronics*, vol. 39, no. 2, pp. 2478–2488, Feb. 2024, doi: 10.1109/TPEL.2023.3334211.

[2] E. Wells, 'Comparing magnetic and piezoelectric transformer approaches in CCFL applications', *Analog Applications Journal*, p. 7, 2002.

[3] A. M. Flynn and S. R. Sanders, 'Fundamental limits on energy transfer and circuit considerations for piezoelectric transformers', *IEEE Transactions on Power Electronics*, vol. 17, no. 1, pp. 8–14, Jan. 2002, doi: 10.1109/63.988662.

[4] A. V. Carazo, '50 years of piezoelectric transformers. Trends in the technology', *MRS Online Proceedings Library Archive*, vol. 785, 2003.

[5] J. D. Boles, J. J. Piel, and D. J. Perreault, 'Enumeration and Analysis of DC–DC Converter Implementations Based on Piezoelectric Resonators', *IEEE Transactions on Power Electronics*, vol. 36, no. 1, pp. 129–145, Jan. 2021, doi: 10.1109/TPEL.2020.3004147.

[6] B. Pollet, G. Despesse, and F. Costa, 'A New Non-Isolated Low-Power Inductorless Piezoelectric DC–DC Converter', *IEEE Trans. Power Electron.*, vol. 34, no. 11, pp. 11002–11013, Nov. 2019, doi: 10.1109/TPEL.2019.2900526.

[7] M. Touhami, G. Despesse, and F. Costa, 'A New Topology of DC–DC Converter Based on Piezoelectric Resonator', *IEEE Transactions on Power Electronics*, vol. 37, no. 6, pp. 6986–7000, June 2022, doi: 10.1109/TPEL.2022.3142997.

[8] J. D. Boles, J. E. Bonavia, J. H. Lang, and D. J. Perreault, 'A Piezoelectric-Resonator-Based DC–DC Converter Demonstrating 1 kW/cm Resonator Power Density', *IEEE Transactions on Power Electronics*, vol. 38, no. 3, pp. 2811–2815, Mar. 2023, doi: 10.1109/TPEL.2022.3217773.

[9] J. Forrester, J. Davidson, and M. Foster, 'Bidirectional inverting piezo resonator-based (BIPR) converter for cell balancing applications', in *2023 IEEE Energy Conversion Congress and Exposition (ECCE)*, Nashville, TN, USA: IEEE, Oct. 2023, pp. 195–201. doi: 10.1109/ECCE53617.2023.10362516.

[10] H. O'Keeffe, M. P. Foster, and J. N. Davidson, 'Piezoelectric-Resonator-Based Power Supply for an Ozone-Generating Dielectric Barrier Discharge Reactor', *IEEE Transactions on Plasma Science*, pp. 3105-3112, 2025, doi: 10.1109/TPS.2025.3598886.

[11] E. Stolt, M. Affolter, Z. Ye, and J. Rivas-Davila, 'Current Mode Control for High Frequency Piezoelectric Resonator-Based DC–DC Converters', *IEEE Transactions on Power Electronics*, vol. 40, no. 9, pp. 12730–12738, Sept. 2025, doi: 10.1109/TPEL.2025.3571873.

[12] S. Moon and J.-H. Park, 'High Power DC–DC Conversion Applications of Disk-Type Radial Mode Pb(Zr,Ti)O_3 Ceramic Transducer', *Jpn. J. Appl. Phys.*, vol. 50, Sept. 2011, doi: 10.1143/JJAP.50.09ND20.

[13] D. Thenathayalan, C. Lee, and J. Park, 'Battery voltage-balancing applications of disk-type radial mode Pb(Zr · Ti)O_3 ceramic resonator', *Jpn. J. Appl. Phys.*, vol. 56, Oct. 2017, doi: 10.7567/JJAP.56.10PD03.

[14] B. Pollet, F. Costa, and G. Despesse, 'A new inductorless DC-DC piezoelectric flyback converter', in *2018 IEEE International Conference on Industrial Technology (ICIT)*, Feb. 2018, pp. 585–590. doi: 10.1109/ICIT.2018.8352243.

[15] J. Forrester, J. N. Davidson, and M. P. Foster, 'Inductorless Step-up Piezoelectric Resonator (SUPR) Converter: a Describing Function Analysis', *IEEE Transactions on Power Electronics*, pp. 12874–12885, 2023, doi: 10.1109/TPEL.2023.3294802.

[16] M. P. Foster, H. I. Sewell, C. M. Bingham, D. A. Stone, D. Hente, and D. Howe, 'Cyclic-averaging for high-speed analysis of resonant converters', *IEEE Transactions on Power Electronics*, vol. 18, no. 4, pp. 985–993, July 2003, doi: 10.1109/TPEL.2003.813763.

[17] H. R. Visser and P. P. J. van den Bosch, 'Modelling of periodically switching networks', in *PESC '91 Record 22nd Annual IEEE Power Electronics Specialists Conference*, June 1991, pp. 67–73. doi: 10.1109/PESC.1991.162655.

[18] E. L. Horsley, A. V. Carazo, N. Nguyen-Quang, M. P. Foster, and D. A. Stone, 'Analysis of Inductorless Zero-Voltage-Switching Piezoelectric Transformer-Based Converters', *IEEE Transactions on Power Electronics*,

vol. 27, no. 5, pp. 2471–2483, May 2012, doi: 10.1109/TPEL.2011.2169431.

[19] Z. Yang, J. Forrester, J. N. Davidson, M. P. Foster, and D. A. Stone, 'Soft Switching Voltage Regulation for Inductorless Piezoelectric Transformers: A Cyclic-Mode Analysis', *IEEE Transactions on Power Electronics*, vol. 38, no. 12, pp. 15645–15658, Dec. 2023, doi: 10.1109/TPEL.2023.3305558.

[20] D. V. Malyna, J. L. Duarte, M. A. M. Hendrix, and F. B. M. van Horck, 'A comparison of methods for finding steady- state solution in power electronic circuits', in *The 4th International Power Electronics and Motion Control Conference, 2004. IPEMC 2004.*, Aug. 2004, pp. 1700-1705 Vol.3. Accessed: Nov. 29, 2023. [Online]. Available: https://ieeexplore.ieee.org/document/1377004

[21] J. Forrester, L. Li, Z. Yang, J. N. Davidson, D. C. Sinclair, I. M. Reaney, M. P. Foster and D. A. Stone, 'Comparison of BSPT and PZT Piezoelectric Ceramic Transformers for High-Temperature Power Supplies', *Adv Eng Mater*, Sept. 2022, doi: 10.1002/adem.202200513.

[22] J. Forrester, L. Li, J. N. Davidson, M. P. Foster, D. A. Stone, D. C. Sinclair and I. M. Reaney , 'Equivalent circuit parameter extraction of low-capacitance high-damping PTs', *Electronics Letters*, Jan. 2020, doi: 10.1049/el.2019.3887.

[23] Z. Yang, J. Forrester, J. N. Davidson, M. P. Foster, and D. A. Stone, 'Resonant Current Estimation and Phase-Locked Loop Feedback Design for Piezoelectric Transformer-Based Power Supplies', *IEEE Trans. Power Electron.*, vol. 35, no. 10, pp. 10466–10476, Oct. 2020, doi: 10.1109/TPEL.2020.2976206.

[24] J. Forrester, M. Foster, and J. Davidson, 'Resonant current estimation and phase-locked loop control system for inductorless step-up single piezo element-based (SUPRC) DC-DC converter', presented at the 48th Annual Conference of the Industrial Electronics Society IECON 2022 Conference, Brussels, Belgium, Oct. 2022.

VIII. APPENDIX

During M6, the SUPR converter can be modelled by the simplified equivalent circuit diagram shown in Fig. 10.

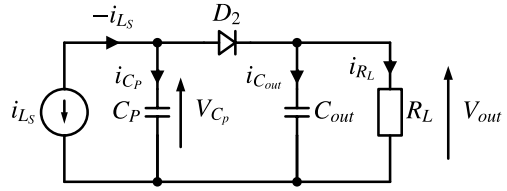

Fig. 10 - Simplified equivalent circuit diagram during M6

Based on this circuit, an equation for the output capacitor voltage (and subsequently the output voltage) in terms of the C_p voltage and diode forward voltage drop is given by

$$v_{\text{out}} = v_{C_\text{p}} - V_{\text{df}} \tag{39}$$

Taking the differential of each term with respect to time gives

$$\dot{v_{\text{out}}} = \dot{v_{C_p}} - \dot{V_{\text{df}}} \tag{40}$$

As the diode forward voltage drop is assumed to be constant in this analysis $\dot{V_{\text{df}}} = 0$ and therefore (40) can be simplified to

$$\dot{v_{\text{out}}} = \dot{v_{C_\text{p}}} \tag{41}$$

Based on Fig. 10, an equation for the resonant current i_{L_S} can be derived

$$-i_{L_\text{s}} = i_{C_\text{p}} + i_{C_\text{out}} + i_{R_\text{L}} \tag{42}$$

Equations for i_{C_p} and $i_{C_{out}}$ can be derived in terms of the relevant capacitor voltages

$$i_{C_\text{p}} = \dot{v_{\text{out}}} C_\text{p}, \qquad i_{C_\text{out}} = \dot{v_{\text{out}}} C_\text{out} \tag{43}$$

Based on these expressions, (42) can be simplified to

$$-i_{L_\text{s}} = \dot{v_{\text{out}}}(C_\text{p} + C_\text{out}) + \frac{v_\text{out}}{R_\text{L}} \tag{44}$$

By then rearranging and dividing (44) by C_out

$$-\frac{i_{L_S}}{C_\text{out}} - \frac{v_\text{out}}{C_\text{out} R_\text{L}} = \dot{v_{\text{out}}}\left(\frac{C_\text{p} + C_\text{out}}{C_\text{out}}\right) \tag{45}$$

Further rearranging gives

$$\dot{v_{\text{out}}} = -\frac{i_{L_S}}{C_\text{p} + C_\text{out}} - \frac{v_\text{out}}{(C_p + C_\text{out}) R_\text{L}} \tag{46}$$